

# Dewetting in immiscible polymer bilayer films

J. Lal,<sup>1,2,3</sup> S. Malkova,<sup>2</sup> M. K. Mukhopadhyay,<sup>4</sup> S. Narayanan,<sup>1</sup>  
A. Fluerasu,<sup>5</sup> S.B. Darling,<sup>6</sup> L. B. Lurio,<sup>3</sup> and M. Sutton<sup>7</sup>

<sup>1</sup>*X-ray Science Division, Argonne National Laboratory, Argonne, IL 60439, USA*

<sup>2</sup>*Intense Pulsed Neutron Source, Argonne National Laboratory, Argonne, IL 60439, USA*

<sup>3</sup>*Department of Physics, Northern Illinois University, DeKalb, IL 60115, USA*

<sup>4</sup>*Department of Physics, University of California, San Diego, La Jolla, CA 92093-0354*

<sup>5</sup>*NSLS-II, Brookhaven National Laboratory, Upton, NY 11973, USA*

<sup>6</sup>*Nanoscience and Technology Division, Argonne National Laboratory, Argonne, IL 60439, USA*

<sup>7</sup>*Physics Department, McGill University, Montréal, H3A 2T8, Canada*

(Dated: May 19, 2016)

We have measured in-situ the dewetting holes in immiscible polymer bilayer films. Using x-ray photon correlation spectroscopy (XPCS) we have been able to probe the holes both at the top surface and the buried interface of the bilayer as dewetting evolved in time. At an early stage, differences in the evolution of velocities between the surface and buried interface indicate that the holes do not penetrate the bottom layer. As the holes increase in size, more material piles up at the rims surrounding the holes and slows down the rims' velocity. The velocity at late stages decays according to a wave vector-dependent power law, which indicates inhomogeneous flows in the film. Our study shows that the universal kinetics of dewetting is largely governed by the evolving slip boundary condition at the buried interface.

PACS numbers: 61.05.cf, 68.60.-p, 82.35.Gh, 83.50.-v

Though dewetting is a common phenomenon in nature, the mechanism governing the retreat of thin polymer films on a substrate began to be understood only recently [1–7]. On a fundamental level, the mechanisms controlling the receding of liquid films on a surface are similar to those involved in phase transitions. De Gennes established a general theory for mobile polymer interfaces during dewetting and wetting [1, 3–5]. Several works studied wetting (spreading) and dewetting using optical techniques and atomic force microscopy (AFM) [8–13]. The experiments are often not in-situ; they mostly probe the surface topography and provide the dewetting velocity of rims around a single hole indirectly. Further, the current theoretical models fail to capture the range of observable effects of dewetting in polymer thin films. During dewetting the polymer chain motion can be complicated due to the presence of large stresses and the importance of nonlinear viscoelastic effects [14].

Various studies explored the dewetting of thin polymer films on solid substrates, where it is sufficient to study the unstable top polymer surface [15]. The more complex dewetting in a polymer bilayer, where the top polymer layer dewets from a deformable polymer underlayer has received less attention [10–13]. Polymer-polymer dewetting presents an experimental challenge since one of the interfaces is buried. Insight from these studies sheds light on the interfacial phenomena of wetting, adhesion and friction in thin polymer films, where mobile borders are involved. The present study focuses on dewetting initiated by nucleation of holes in supported viscoelastic bilayer films.

Previous work on single holes [1] has shown that capillarity represents the main driving force for spreading

or dewetting. The dewetting is opposed by viscous or viscoelastic dissipation within the polymer film and frictional losses at the substrate. When the increase in dewetting driving force is smaller than the increase in frictional force, the fluid starts to collect in a “rim” close to the moving three-phase contact line [9].

A full statistical picture of the temporal evolution of the rims is hard to obtain by optical microscopy and AFM. There have been attempts to probe spreading of droplets and dewetting in films using x-ray scattering [15–17]. X-ray photon correlation spectroscopy (XPCS) is an experimental method enabled by high-brightness third-generation synchrotron sources ideally suited to measure mesoscale dynamics in condensed-matter systems [18, 19]. In the present work, two-time correlation functions (TTCFs) measured by XPCS in grazing incidence [21] provide in-situ snapshots of the dewetting process, particularly the dewetting velocity of the rims at the top and buried interface.

The system studied was a poly(4-bromo styrene) (PBrS) thin film deposited on an immiscible and non-wettable polystyrene (PS) sublayer on a silicon substrate. Monodisperse PS (molecular weight  $M_w = 207$  kDa from Pressure Chemical) and PBrS ( $M_w = 350$  kDa, the fraction of brominated monomers was 0.89) were used in these experiments. The bilayers were prepared by spin coating PBrS layers of thickness 1000 Å, 700 Å and 400 Å onto a glass slide and then floated from de-ionized water onto the 1000 Å PS sublayer, which was previously deposited on pre-cleaned 15 × 15 mm silicon wafers. Viscous polymers (PBrS/PS bilayers) with high-molecular weight and thick films ( $\sim 1000$  Å) were chosen to slow down the kinetic processes and enable in-situ studies [13]. For

these thick films, the holes were on average separated by several microns so that they were not affected by neighbouring holes.

The PBrS/PS bilayers are metastable and, if heated above the glass transition temperatures, the top surface dewets from the PS-coated substrate. This agrees with previous PEEM measurements [20] on PBrS/PS bilayers, which showed that the diffusion and flow parallel to the interfaces is faster for both PS and PBrS than the diffusion of PS perpendicular to the PS/PBrS interface. As the PS and PBrS are highly immiscible, the diffusion of PS through the PBrS layer is severely hindered.

Optical images indicate [21] heterogeneous nucleation due to non-equilibrated conformational states and residual stresses [6]. The radial size of the holes measured by AFM varied between 8–14  $\mu\text{m}$  (depending on the annealing time and on the particular hole). The AFM data [21] show a clear rim after 12 hours formed from the material collected from the hole. Symmetric rims are observed around small young holes ( $\sim 10 \mu\text{m}$ ) and asymmetric rims are found around large mature holes ( $\sim 30 \mu\text{m}$ ) irrespective of the thickness of the top bilayer.

Grazing-incidence XPCS experiments were performed with beamsized 20  $\mu\text{m}$  at the sector 8-ID-I beamline at the Advanced Photon Source, Argonne National Laboratory. The samples were held at 170°C, above the glass transition of the polymers, and the evolving off-specular diffuse scattering was monitored as a function of annealing time using a charge-coupled device (CCD) detector with 22  $\mu\text{m}$  pixels located 4.8 m downstream of the sample. Each frame was recorded with an exposure time of 0.2 s and a time interval between successive frames of 8.32 s. The zero of the waiting time  $t_w$  corresponded to the initial temperature anneal from room temperature to 170°C. XPCS data was collected until late in the dewetting process ( $t_w \sim 7$  hours) in 1.2 hours time steps, alternating between measurements of the dynamics at the top surface and the buried interface. For x-rays incident at an angle ( $\theta_{in} = 0.175^\circ$ ) smaller than the critical angle of the top layer ( $\alpha_c = 0.191^\circ$  for PBrS), all of the scattering originates from the top layer. Following a reverse standing-wave method described in Refs. [22, 23], a larger incident angle was chosen ( $\theta_{in} = 0.225^\circ$ ) to yield scattering dominated by the buried interface of the bilayer [21]. For  $\theta_{in} = 0.175^\circ$  the footprint of the x-ray beam was approximately 7 mm so that around 250 holes were illuminated (assuming an average hole size of 10  $\mu\text{m}$  and spacing between holes  $\sim 20 \mu\text{m}$ ).

The non-stationary dynamics associated with the out-of-equilibrium dewetting process were measured by means of TTCFs (Fig. 1) [24],

$$C(q, t_1, t_2) = \frac{\langle I(q, t_1)I(q, t_2) \rangle}{\langle I(q, t_1) \rangle \langle I(q, t_2) \rangle}. \quad (1)$$

Examples of TTCFs averaged over a region of pixels with the same in-plane component of the scattering wave vec-

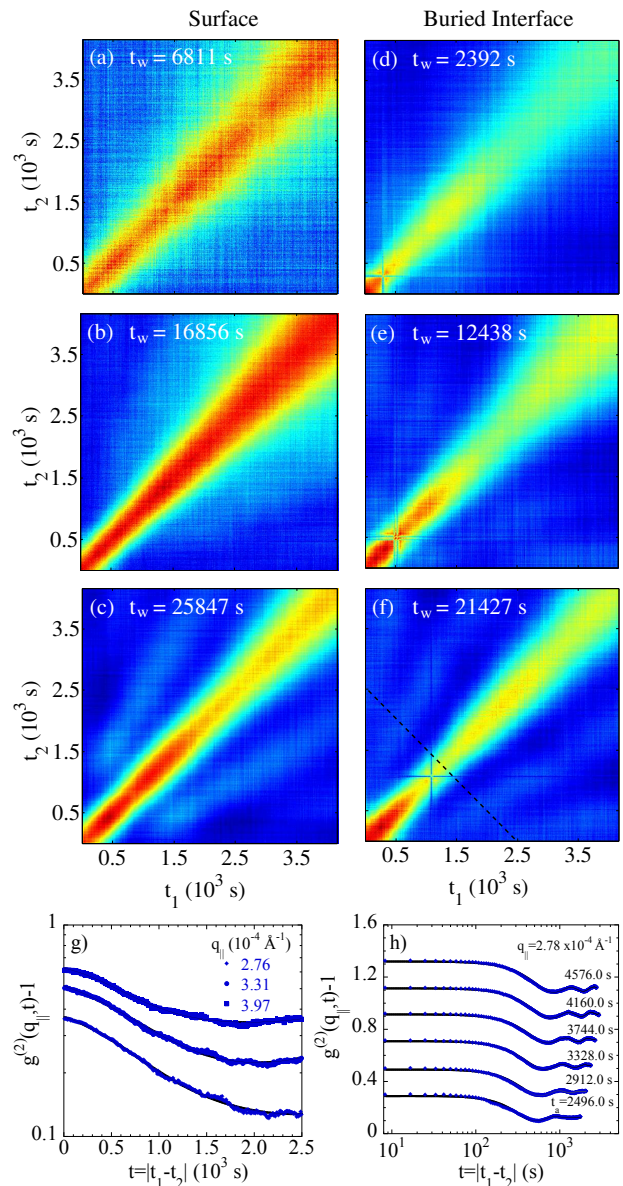


FIG. 1. TTCFs measured from the top surface and buried interface of the bilayer at  $q_{\parallel} \sim 2.78 \times 10^{-4} \text{ \AA}^{-1}$ . The  $t_w$  for the measured TTCFs are (a) 6811 s, (b) 16856 s, (c) 25847 s and (d) 2392 s, (e) 12438 s, (f) 21427 s, respectively.  $g^{(2)}(q_{\parallel}, t) - 1$  for the buried interface (g) at  $t_a = 4576$  s and  $t_w = 2392$  s and (h)  $t_w = 21427$  s as a function of  $t = |t_1 - t_2|$ . Solid lines in (g) and (h) are fits based on Eq. (3). For clarity, the curves in panel (h) starting with the second one were shifted up in multiples of 0.2.

tor  $q_{\parallel} \sim 2.78 \times 10^{-4} \text{ \AA}^{-1}$  are shown in Figs. 1(a)-(f). The natural variables describing TTCFs are the ‘‘aging time’’  $t_a = (t_1 + t_2)/2$ , measured along the  $t_1 = t_2$  diagonal and the time difference  $t = |t_1 - t_2|$  corresponding to the distance from the same diagonal. The ‘‘one-time’’ slices  $t_a = \text{const}$  [dotted line in Fig. 1(e)] are fitted based on Eq. (3) below (solid lines), and non-stationary effects can be observed by fitting successive slices representing

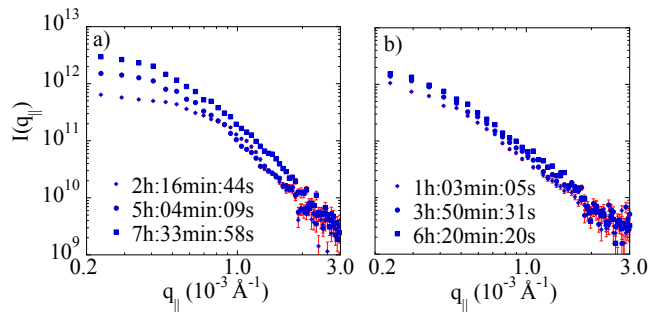


FIG. 2. Average static diffuse scattering from (a) surface and (b) buried interface of the bilayer corresponding to TTCFs in Figs. 1(b), (c), (e) and (f).

$g^{(2)}(q_{\parallel}t) - 1$  [Fig. 1(h)].

Assuming that the dewetting ring can be modeled by a rim velocity that is slowly varying so that the change in structure (within  $t_a = 1.2$  hours) can be ignored, a variant of Fuller's model [25] can be used to describe the data, yielding the normalized intermediate scattering function  $g^{(1)}(q_{\parallel}t)$  in terms of a Bessel function  $J_0$ . Using  $q_{\parallel}$  and the in-plane velocity  $V_0$  of the rims associated with the dewetting process,  $g^{(1)}(q_{\parallel}t)$  can be expressed as [21]

$$g^{(1)}(q_{\parallel}t) = \frac{1}{2\pi} \int_0^{2\pi} e^{i\sqrt{A^2+B^2} \sin(\phi+\psi)} d\phi = J_0(q_{\parallel}V_0t). \quad (2)$$

This is related to the intensity autocorrelation function  $g_2(q_{\parallel}t)$  via the Siegert relationship,  $g_2(q_{\parallel}t) = 1 + \beta|g_1(q_{\parallel}t)|^2$ , where  $A$ ,  $B$  and  $\psi$  are defined in Ref. [21] and  $\beta$  is the optical contrast. Thus,

$$g^{(2)}(q_{\parallel}t) = \beta J_0^2(V_0q_{\parallel}t) + 1. \quad (3)$$

The characteristic oscillations reflecting the asymptotic form of  $J_0 \sim \sin(q_{\parallel}V_0t)/(q_{\parallel}V_0t)$  can be clearly seen for the time slices in Fig. 1(h), thus demonstrating the validity of the model (3).

To take account of polydispersity in the sizes of holes (thus, the rims around them) indicated by optical micrographs [21], a Gaussian distribution of velocities  $\frac{1}{\sigma\sqrt{2\pi}}e^{-(V_0-V)^2/2\sigma^2}$  was assumed with mean velocity  $V$  and variance  $\sigma$ . The Gaussian was convoluted with the Bessel function, and a numerical integration was performed at each time step for successive slices of  $g^{(2)}(q_{\parallel}t) - 1$  to get the mean velocity  $V$ . The variance  $\sigma$  reflects the average distribution of velocities within rims of different sizes hence samples an average rim size [21].

The time average "static" diffuse scattering from the top surface corresponding to Fig. 1(b), (c) is shown in Fig. 2(a) and that corresponding to the buried interface Fig. 1(e), (f) is shown in Fig. 2(b). After five hours, a large change of static diffuse intensity is observed from the top surface, which indicates that a significant number of rims around holes have formed. Meanwhile, the

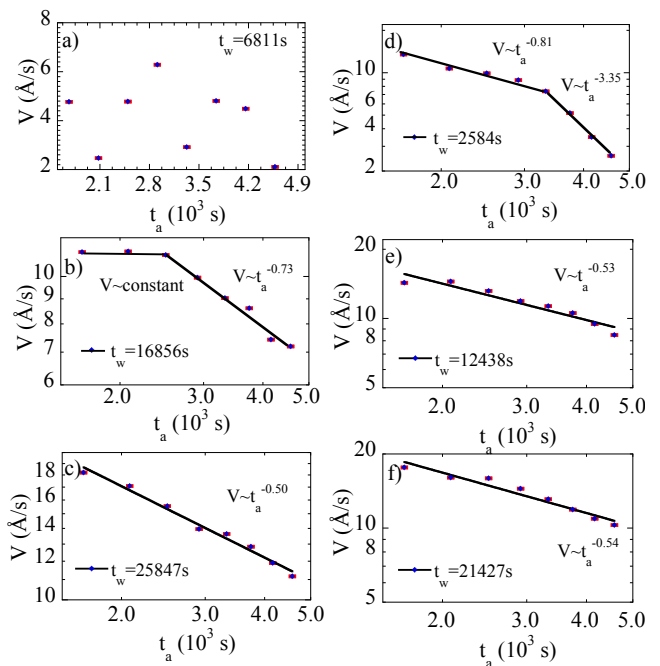


FIG. 3. Mean velocities  $V$  as a function of  $t_a$  for increasing values of  $t_w$ . Results for the top surface are shown in panels (a), (b), (c) and from the buried interface in panels (d), (e), (f) for  $q_{\parallel} \sim 2.78 \times 10^{-4} \text{ \AA}^{-1}$ .

static diffuse intensity from the buried interface shows very small increases at low  $q_{\parallel}$  during this time [Fig. 2(b)] which implies that the interface tension slightly decreases [22]. The latter can be related to the very small interdiffusion between the immiscible PS and PBrS polymer chains (on a segmental level). This small roughening of the buried PS/PBrS interface in time can suppress slippage and lead to asymmetric rim profiles [21, 26]. Experiments [27, 28] showed that chain interdiffusion at the interface affects the friction. The slippage length is  $b = \eta/k$ , with polymer viscosity  $\eta$  and friction coefficient  $k$ . The decrease of  $b$  with increasing  $k$  induces a decrease of the maximum rim width  $w = \sqrt{b\hbar}$ , where  $\hbar$  is the thickness of the film [29], finally leading to asymmetric rims [9, 21].

Figure 3 shows the mean velocities  $V$  for  $q_{\parallel} \sim 2.78 \times 10^{-4} \text{ \AA}^{-1}$  as a function of  $t_a$  and for increasing values of  $t_w$  resulting from fits based on Eq. (3). Data for the top surface [Figs. 3(a), (b), (c)] and the buried interface [Figs. 3(d), (e), (f)] correspond to the TTCFs in Figs. 1(a), (b), (c) and Figs. 1(d), (e), (f). The estimated error in  $V$  is extremely small. The data suggests that a large number of holes form very early ( $\lesssim 1$  hour) and that later times are dominated by scattering from the rims of these holes, and not from capillary waves as has been seen in other polymer systems [23], except in the very beginning  $t_w = 2392\text{s}$  at the buried interface [Fig. 3(d)], where  $V \sim t_a^{-3.35}$  is associated with interface broadening due

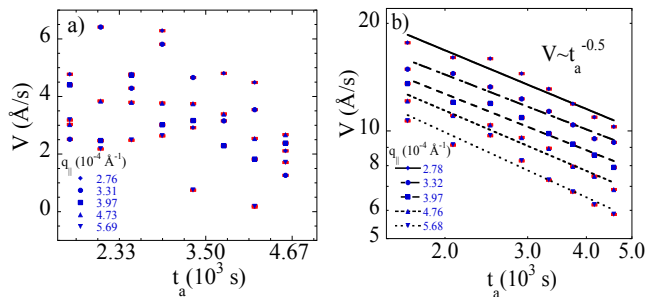


FIG. 4. Mean velocity  $V$  as a function of  $t_a$  for different wave vectors  $q_{||}$  for (a) 1000 Å top surface at  $t_w = 6811$  s and (b) buried interface of the bilayer at  $t_w = 21427$  s.

to capillary waves [1, 22]. Initial XPCS measurements probe a regime where there are many holes opening and dynamics are chaotic, due to a superposition of mature and immature holes [Fig. 3(a)]. Later measurements ( $\gtrsim 3$  hours) show a more stable regime characteristic of hole growth. However, differences in scattering between the top interface and the buried interface of the bilayer indicate that most holes have not fully penetrated down to the substrate, and thus appear significantly different depending on which height in the sample is probed. Different areas of the sample may also have holes that initiated at different absolute times. Translation to different parts of the sample, in order to minimize x-ray damage, changes the hole distribution and may catch holes at different states in their time evolution (Fig. 3).

We note that the order of magnitude of the velocity  $V$  (Fig. 3) can be estimated as follows. In most capillary phenomena in the viscous regimes [1], the characteristic velocity is a function of the liquid; it varies as  $V^* = \gamma/\eta$ . Here  $\gamma$  is the effective interface tension between PS and PBrS [15, 21] and  $\eta$  is the average viscosity of PS and PBrS, yielding  $V^* \sim 7.29$  Å/s.

The results in Fig. 3 agree with single-hole opening dynamics [14, 29]. The stress  $\sigma_s$  due to the capillary forces is the spreading parameter  $S$  ( $-5.4 \times 10^{-3}$  N/m) divided by the thickness of the PBrS film  $h$  (here 1000 Å) [14, 29], yielding  $0.54 \times 10^5$  N/m<sup>2</sup>, which is comparable to the bulk plateau modulus of PBrS ( $G \sim 1.94 \times 10^5$  N/m<sup>2</sup>, based on entanglement molecular weight  $M_e = 29845$  g/mol [30]). As the hole opens, the whole film is elastically deformed by these capillary forces  $S$  acting at the hole periphery. The small-amplitude oscillations in Fig. 1(g) and [21] with 300 s period, which are not captured by Eq. (3), may correspond to a higher initial hole opening velocity  $\sim 60$  Å/s. As long as the hole radius  $r < w$ , viscous dissipation dominates over dissipation due to interfacial friction. During this early stage the dewetted hole size increases [Fig. 2(a)], up to  $V \simeq \text{const}$  [Fig. 3(b)]. This is followed by a power law  $V \sim t_a^{-0.73}$ , where a slow rim build-up takes place [6]. When  $r > w$ , friction dominates over viscous dissipation. At still later times  $t_w = 25847$  s,

after a maximum rim size is attained [6],  $V \sim t_a^{-0.50}$  was observed [Fig. 3(c)]. The velocity decrease with increasing time reflects the viscoelasticity of the polymer, the nonlinear friction at the interface of PBrS/PS and the extent of residual stresses present in the film [6, 31, 32]. Similar power law behavior  $V \sim t_a^{-\alpha}$ , where  $\alpha$  is between 0.5 and 1.0, is seen for the bottom layer [Figs. 3(d), (e), (f)].

Figure 4 shows the velocity as a function of  $t_a$  for different values of  $q_{||}$ . Figures 3(a) and 4(a) show a randomly varying velocity as a function of  $t_a$  at the top surface of the 1000 Å film at the earliest time. This evolves towards a  $q_{||}$  dependent power law decay at later times as shown for the top interface in Fig. 3(c) and for the buried interface in Fig. 4(b). The  $q_{||}$  dependent velocity indicates inhomogeneous flows in the film. These results further indicate that wider younger rims [21] move faster and scatter at low  $q_{||}$ , whereas more mature slower rims, which are smaller in width [21], scatter at larger  $q_{||}$  [Fig. 4(b)].

The  $q_{||}$  dependence  $V \sim q_{||}^{0.8}$  is seen for all film thicknesses  $h$  (Fig. 5). The data also shows that  $V$  decreases with decreasing  $h$ . An explanation for this behavior is that in the beginning the dewetting rates are markedly higher for thinner films [9]. Decreasing thicknesses thus show the dewetting history at later times. This implies that at the buried interface the 400 Å and 700 Å top layers have a larger contribution to the more mature rims (with smaller  $V$ ) than the 1000 Å layer.

In conclusion, in-situ snapshots of the diffuse scattering at the top and buried interface of immiscible polymer bilayer films provide a detailed probe of dewetting through the evolution of the rim velocities obtained from TTCFs. The  $q_{||}$  dependent velocities observed here indicate inhomogeneous flows in the film. As the holes get bigger, more material piles up at the rim [9], thus requiring the velocity to slow down. Further, changes in the static diffuse scattering point to the important role played by interface evolution and hence friction (suppressing slippage) in defining the asymmetric rim shapes [21, 28]. The power laws observed here at late times for the average velocity are similar to those observed in AFM studies of single dewetting holes in viscoelastic polymer films deposited on a very thin polymer cushion layer on silicon substrates [6, 32]. Previously it was found that merely a slip-boundary condition at the polymer-solid interface can lead to an asymmetric rim profile [26]. Our work shows that the slip and its evolution at the polymer-polymer interface of bilayers [23] and similar engineered interfaces [6, 26, 32] is the most important condition for the universality of dewetting kinetics seen in viscoelastic thin polymer films.

This research used resources of the Advanced Photon Source and the Center for Nanoscale Materials, U.S. Department of Energy (DOE) Office of Science User Facilities operated for the DOE Office of Science by Argonne National Laboratory under Contract No. DE-

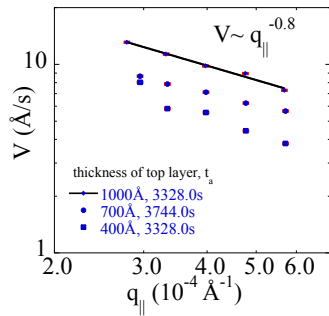


FIG. 5. Mean velocity  $V$  at the buried interface as a function of  $q_{\parallel}$  for the  $t_a$  indicated. The  $t_w$  for the 1000 Å top layer is 21427 s, for the 700 Å is 24113 s and for the 400 Å is 15364 s.

AC02-06CH11357.

- 
- [1] P. G. de Gennes, F. Brochard-Wyart, and D. Quere, *Capillarity and Wetting Phenomena: Drops, Bubbles, Pearls, Waves*, (Springer, New York, 2004).
- [2] S. Chandran and G. Reiter, Phys. Rev. Lett **116**, 088301 (2016).
- [3] M. E. R. Shanahan, J. Phys. D: Appl. Phys. **21**, 981 (1988).
- [4] P. G. de Gennes, Rev. Mod. Phys. **57**, 827 (1985).
- [5] F. Brochard-Wyart, P. Martin, and C. Redon, Langmuir **9**, 3682 (1993).
- [6] G. Reiter, M. Hamieh, P. Damman, S. Sclavons, S. Gabriele, T. Vilmin, and E. Raphael, Nat. Mater. **4**, 754 (2005).
- [7] P. Damman, S. Gabriele, S. Coppee, S. Desprez, D. Villers, T. Vilmin, E. Raphael, M. Hamieh, S. Al Akhrass, and G. Reiter, Phys. Rev. Lett. **99**, 036101 (2007).
- [8] F. Heslot, N. Fraysse, and A. M. Cazabat, Nature **338**, 640 (1989).
- [9] G. Reiter, Adv. Polym. Sci. **252**, 29 (2013).
- [10] P. Lambooy, K. C. Phelan, O. Haugg, G. Krausch, Phys. Rev. Lett. **76**, 1110 (1996).
- [11] K. Kostourou, D. Peschka, A. Münch, B. Wagner, S. Herminghaus, and R. Seemann, Chem. Eng. Process. **50**, 531 (2011).
- [12] R. A. Segalman and P. F. Green, Macromolecules **32**, 801 (1999).
- [13] D. Slep, J. Asselta, M. H. Rafailovich, J. Sokolov, D. A. Winesett, A. P. Smith, H. Ade, and S. Anders, Langmuir **16**, 2369 (2000).
- [14] G. Reiter, Phys. Rev. Lett. **87**, 186101 (2001).
- [15] M. Sferrazza, M. Heppenstall-Butler, R. Cubitt, D. Bucknall, J. Webster, and R. A. L. Jones, Phys. Rev. Lett. **81**, 5173 (1998).
- [16] J. Daillant, J. Benattar, L. Bosio and L. Leger, Europhys. Lett. **6**, 431 (1988).
- [17] P. Müller-Buschbaum, P. Vanhoorne, V. Scheumann, and M. Stamm, Europhys. Lett. **40**, 655 (1997).
- [18] G. Grübel, A. Madsen, and A. Robert, in *Soft Matter Characterization*, edited by R. Borsali and R. Pecora, pp 953-995, (Springer, New York, 2008).
- [19] M. Sutton, in *Third Generation Hard X-Ray Synchrotron Radiation Sources*, edited by D. Mills, (Wiley, New York, 2002).
- [20] H. Ade, D. A. Winesett, A. P. Smith, S. Anders, T. Stammer, C. Heske, M. H. Rafailovich, J. Sokolov, and J. Stöhr, Appl. Phys. Lett. **73**, 3775 (1998).
- [21] See Supplementary Materials.
- [22] X. Hu, X. Jiao, S. Narayanan, Z. Jiang, S. K. Sinha, L. B. Lurio, and J. Lal, Eur. Phys. J. E **17**, 353 (2005).
- [23] X. Hu, Z. Jiang, S. Narayanan, X. Jiao, A. R. Sandy, S. K. Sinha, L. B. Lurio, and J. Lal, Phys. Rev. E **74**, 010602 (2006).
- [24] M. Sutton, K. Laaziri, F. Livet, and F. Bley, Opt. Express, **11**, 2268 (2003).
- [25] G. G. Fuller, J. M. Rallison, R. L. Schmidt, and L. G. Leal, J. Fluid Mech. **100**, 555 (1980).
- [26] O. Bäumchen, R. Fetzer, and K. Jacobs, Phys. Rev. Lett. **103**, 247801 (2009).
- [27] S. Coppee, S. Gabriele, A. M. Jonas, J. Jestin and P. Damman, Soft Matter **7**, 9951 (2011).
- [28] F. Ziebert and E. Raphael, Europhys. Lett., **86**, 46001 (2009).
- [29] F. Brochard-Wyart, G. Debregeas, R. Fondécave, and P. Martin, Macromolecules **30**, 1211 (1997).
- [30] J. T. Seitz, J. Appl. Polym. Sci. **49**, 1331 (1993).
- [31] T. Vilmin and E. Raphael, Europhys. Lett. **72**, 781 (2005).
- [32] P. Damman, N. Baudelet and G. Reiter, Phys. Rev. Lett. **91**, 216101, (2003).